Reaction mechanisms and kinetics of the O-2 addition pathways to the main thiophene-OH adduct: a theoretical study

DOI: 10.3184/146867816X14754978258571
Handle: http://hdl.handle.net/1942/22991

Reaction mechanisms and kinetics of the O_2 addition pathways upon the main thiophene-OH adduct: A theoretical study

Abolfazl Shiroudi, Michael S. Deleuze*

Center of Molecular and Materials Modelling, Hasselt University, Agoralaan, Gebouw D, B-3590 Diepenbeek, Belgium

Abstract

Density Functional Theory along with the ωB97XD and UM06-2*x* exchange-correlation functionals has been used to study the reaction mechanisms and kinetics of atmospheric oxidation of the main (kinetically dominant) thiophene-OH adduct $[C_4H_4S\text{-}OH]^{\bullet}$ (R1) by molecular oxygen in its triplet electronic ground state. Kinetic rate constants and branching ratios under atmospheric pressure and in the fall-off regime have been calculated by means of transition state theory (TST), variational transition state theory (VTST) and statistical Rice–Ramsperger–Kassel–Marcus (RRKM) theory. In line with the computed energy profiles, the dominant process under both a thermodynamic and kinetic control of the reaction is O_2 addition at the C_5 position in *syn* mode. The computed branching ratios indicate that the regioselectivity of the reaction decreases with increasing temperatures and decreasing pressures.

Keywords: thiophene; hydrogen bonding; natural bond orbital analysis; reaction mechanisms; chemical kinetics; RRKM theory.

* Corresponding author: Tel: +32-11-268303 ; E-mail: michael.deleuze@uhasselt.be

1. Introduction

Polycyclic aromatic sulfur heterocycles (PASHs) are present in most petroleum and coal products, combustion products, air particulates, etc [1−3]. There is a considerable interest in the removal of sulfur containing compounds from fossil fuels in order to decrease sulfur dioxide emissions. The presence of sulfur compounds in fuels is undesirable also from the viewpoint of catalyst poisoning during refining and, consequently, desulfurization processes are a very active research area. Many experiments suggest that aromatics are the most difficult compounds to desulfurize [4].

Among the reduced sulfur compounds released into the atmosphere from both natural and industrial sources, natural emissions of COS, H_2S and CH_3SCH_3 dominate, but other species like thiophene, tetrahydrothiophene and diethylsulfide have also to be considered [5]. Kinetic and mechanistic data for the reactions of sulfur compounds such as thiophene with important oxidant species like ozone (O_3), hydroxyl ($OH^{\bullet}$) and nitrate ($NO_3^{\bullet}$) radicals are required for evaluating their residence times as well as the ultimate fates of these compounds in the atmosphere [6−16]. Since during day-time the most important atmospheric chemical loss processes involve reactions with ozone and hydroxyl radicals, kinetic and mechanistic data for these reactions are especially needed in order to develop physico-chemical models of atmospheric pollution [14−18], which will contribute to improving our understanding of sulfur cycle in the atmosphere [19]. Hydroxyl radicals play indeed a key role in determining the oxidation power of the atmosphere [20].

Thiophene is nowadays becoming of increasing importance both in combustion and in atmospheric chemistry as a result of the development of new energy technologies related to conversion or combustion of coal, shale oil and petroleum [21,22]. Under ambient conditions, the oxidation of aromatic rings in the gas phase by OH radicals yields hydroxycyclohexadienyl-type radicals, which can back decompose to the reactants or further react with NO_2 or O_2 to yield highly carcinogenic derivatives [23−32]. In severely polluted urban areas, it is known that the reactions of OH−monocyclic aromatic hydrocarbon adducts with O_2 dominate under ambient conditions [29].

In a preceding article [33], we have studied the first reaction steps involved in the oxidation mechanisms of thiophene which are initiated by OH radicals. The OH addition pathway which dominates under inert conditions (Ar) at temperatures ranging from 298 to 471 K under a kinetic

control of the reaction is the OH addition process onto a carbon atom which is adjacent to the sulfur atom ($[C_4H_4S\text{-}OH]^\bullet$, referred from here and henceforth as the R1 adduct – see Fig. 1). Under atmospheric conditions, this intermediate energized adduct is expected to react primarily with triplet molecular oxygen, to form $[C_4H_4S\text{-}OH]^\bullet\text{–}O_2$ peroxy radicals. O_2 addition onto the R1 energized adduct can occur at three different positions, namely onto the C_3, C_4, and C_5-positions (P1–P6, see Fig. 1). Depending on the relative (*syn* or *anti*) location of the hydroxyl and peroxy substituents with respect to the attacked ring scaffold, this third reaction step leads on total to six different isomers (Fig. 1), which are referred further to as the R1-*i*OO-*anti*/*syn* (*i*=3–5) radicals. Similar reactions of O_2 with [OH–benzene]$^\bullet$ [34–37], [OH–naphthalene]$^\bullet$ [38] and [OH–toluene]$^\bullet$ [39] adducts are known to proceed first through a reversible addition of O_2 to the OH–aromatic adduct to form an [OH-aromatic]–O_2 peroxy radical [32]. In analogy with these works, a pre-equilibrium reversible bimolecular reaction step will therefore also be considered in our model.

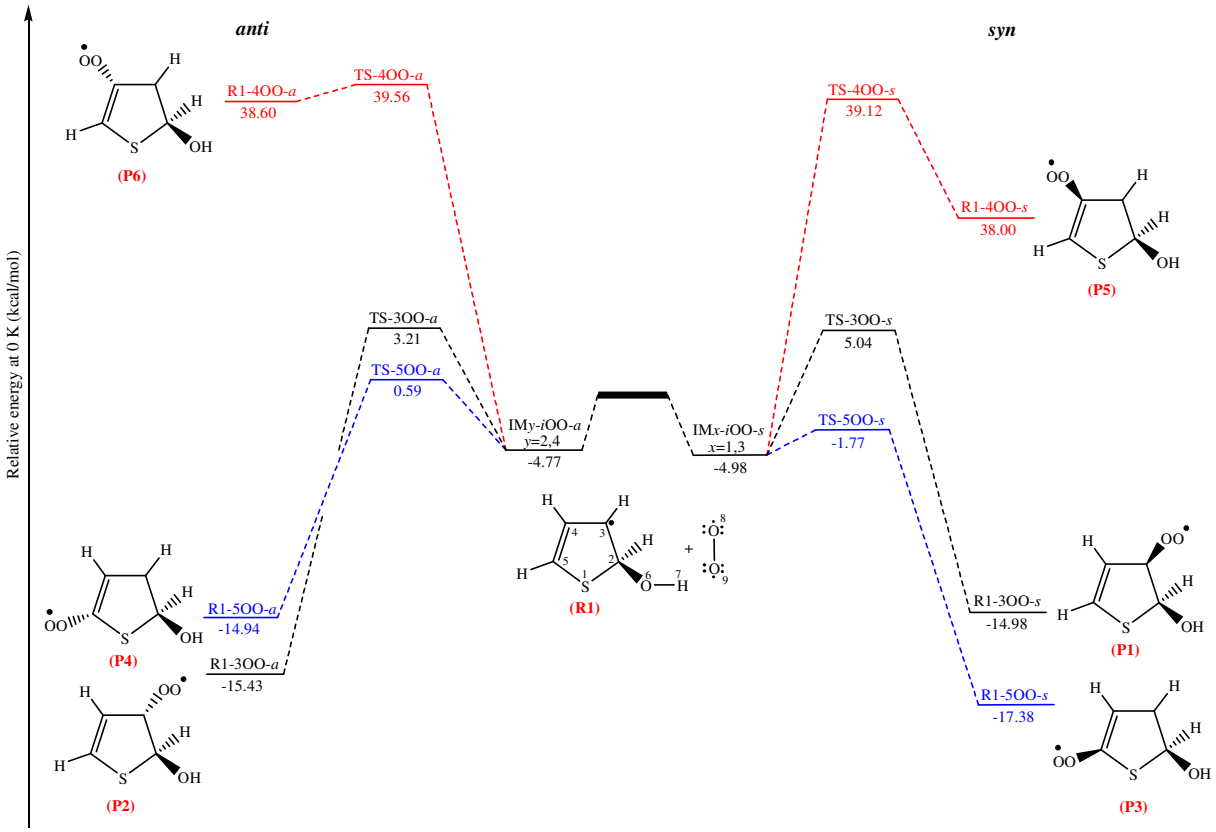

Fig. 1. Potential energy diagram for the considered reaction pathways at the UM06-2*x*/aug-cc-pVTZ level of theory.

Theoretical kinetic rate constants for all unimolecular and bimolecular reaction steps that are involved in the addition of O_2 onto the R1 adduct will be supplied, along with global rate constants and branching ratios at temperatures ranging from 298 to 471 K and various pressures. In this purpose, use shall be made of standard and variational transition state theory (TST, VTST) [40–49] as well as statistical Rice–Ramsperger–Kassel–Marcus (RRKM) theory [48–50], in conjunction with the dispersion-corrected ωB97XD [51] and the UM06-2*x* [52,53] exchange-correlation functionals and Dunning's augmented correlation consistent polarized valence basis set of triple zeta quality (aug-cc-pVTZ) [54]. Note that the UM06-2*x* functional has been especially designed for accurate studies of chemical reactions, both from a thermodynamic and kinetic viewpoint, whereas a main advantage of the ωB97XD functional is a consistent treatment of dispersion forces. At last, in the present work, we will also strive to supply further qualitative chemical insights into the involved reaction mechanisms, by analyzing results obtained by means of natural bond orbital (NBO) analysis [55,56].

2. Computational details

All calculations that are discussed in the present work have been performed using the Gaussian 09 package of programs [57]. All reported calculations have been carried out at the Flemish Supercomputer Centre, in Heverlee (Leuven, Belgium). Molecular structures were visualized using Gauss View [58]. The molecular structures and harmonic vibrational frequencies of all stationary points of interest were calculated using density functional theory along with the dispersion corrected ωB97XD [51] and the UM06-2*x* exchange-correlation functionals [52,53], in conjunction with Dunning's correlation-consistent basis set of triple-ζ quality augmented with diffuse functions (aug-cc-pVTZ basis set) [54].

Frequency calculations were carried out to check the nature of the identified stationary points. The connections between transition states and the corresponding energy minima have been verified according to intrinsic reaction coordinate (IRC) calculations [59] that were carried out at the B3LYP/6-31G(d,p) level, by means of the second-order Gonzalez-Schlegel integration method [60,61]. Thermodynamic state functions (*H*, *S*, *G*) were obtained from these frequency calculations and from canonical partition functions obtained for an ideal polyatomic gas under a pressure of 1 atm using the standard RRHO (rigid rotor harmonic oscillator) approximation and

Boltzmann statistics (see refs 62 and 63 or any textbook of molecular statistical mechanics for a detailed review of the underlying theory).

In the present work, the O_2 addition process onto the $[C_4H_4S–OH]^\bullet$ adduct (R1) has been analyzed according to a two-step reaction mechanism [64], involving first a fast pre-equilibrium between the reactants (R1+O_2) and a pre-reactive complex $[C_4H_4S\text{-}OH\ldots O_2]^\bullet$ (IM), followed by the irreversible formation of the thiophene peroxy radicals $[C_4H_4SOH–O_2]^\bullet$:

$$\text{step 1: } \left[C_4H_4S\text{-}OH\right]^\bullet + O_2 \underset{k_{-1}}{\overset{k_1}{\rightleftharpoons}} \left[C_4H_4S\text{-}OH\ldots O_2\right]^\bullet$$

$$\text{step 2: } \left[C_4H_4S\text{-}OH\ldots O_2\right]^\bullet \xrightarrow{k_2} \text{R1-}i\text{OO-}anti/syn\,(i\text{=3-5})$$

In the above reactions, k_1 is the kinetic rate constant which characterizes the forward bimolecular reaction step (in cm^3 $molecule^{-1}$ s^{-1}), whereas k_{-1} and k_2 correspond to the backward and forward unimolecular reaction rate constants (in s^{-1}). The following expression for the global rate constant is obtained according to a steady-state analysis [64]:

$$k_{\text{overall}} = \frac{k_1 k_2}{k_{-1} + k_2} \tag{1}$$

In general, the energy barrier for k_{-1} has about the same height as that for k_2. However, the entropy change for the reverse reaction (IM→R1+O_2) must be much larger than that for the formation of the products [IM→R1-*i*OO-*anti*/*syn* (*i*=3–5)], because six vibrational modes are converted into three rotational modes and three translational modes. It follows that k_2 must be negligible compared with k_{-1} (an assumption which has been checked in details according, to RRKM calculations – see all data reported in the Supporting Information). The global rate constant (k_{overall}) can thus be reliably estimated as follows:

$$k_{overall} = K_c k_2 \tag{2}$$

where K_c=k_1/k_{-1} is the equilibrium constant for the fast pre-equilibrium between the reactants and the pre-reactive complex (step 1):

$$K_c = \frac{\left[C_4H_4S\text{-}OH\ldots O_2\right]^\bullet}{\left[C_4H_4S\text{-}OH\right]^\bullet \left[O_2\right]} \tag{3}$$

Upon using statistical thermodynamics (see in particular eq. 26.3–20 in ref. 65), the equilibrium constant of the fast pre-equilibrium between the reactants and the pre-reactive complex can be obtained by means of the following relationship:

$$K_c = \frac{Q_{IM}}{Q_{R1}.Q_{O_2}} \times \frac{V_m(T)}{N_{Av}} \times \exp\left(-\frac{(E_{IM} - E_{R1} - E_{O_2})}{RT}\right) \quad (4)$$

where N_{Av} and R represent the Avogadro number and the ideal gas constant, respectively, and where $V_m(T)=RT/P$ the molar volume of an ideal gas at the considered temperature (T) and pressure (P), the kinetic rate constant characterizing the unimolecular dissociation reaction of the pre-reactive complex have been obtained at temperatures ranging from 298 to 471 K by means of transition state theory, an approach which is in principle valid only in the high-pressure limit ($P \rightarrow \infty$) and for reactions involving large enough reaction barriers corresponding to well-defined transitions states [40–47]:

$$k_2 = \kappa(T) \times \frac{\sigma k_B T}{h} \times \frac{Q_{TS}}{Q_{IM}} \times \exp\left(-\frac{(E_{TS} - E_{IM})}{RT}\right) \quad (5)$$

TST has also been used to readily evaluate the global bimolecular kinetic rate constants for the whole process, using the following equation [66–68]:

$$k_{overall} = \kappa(T) \times \frac{\sigma k_B T}{h} \times V_m(T) \times \frac{Q_{TS}(T)}{Q_A(T).Q_B(T)} \times \exp\left(-\frac{(E_{TS} - E_A - E_B)}{RT}\right) \quad (6)$$

In the two preceding equations, σ is the reaction symmetry number, $\kappa(T)$ denotes the Wigner's tunneling factor [69], and k_B and h represent the Boltzmann's and Planck's constants, respectively. In these equations, Q_A, Q_B, and Q_{TS} correspond to the total molecular partition functions for the isolated reactants (A ≡ R1, B ≡ O_2) and to the transition state associated to the unimolecular dissociation reaction (step 2), respectively. E_A, E_B and E_{TS} are the corresponding energies (including zero-point vibrational energy contributions). Vibrational partition functions were computed using the vibrational ground state as energy reference, because the computed energy differences account for zero-point vibrational energies. Tunneling corrections were assumed to be insignificant, considering the size of the reacting molecules. Note that, in practice, standard atmospheric pressures (1 bar) are usually considered to be large enough for reliably calculating kinetic rate constants by means of TST. Since some of the studied reaction pathways involve loose transition states corresponding to small energy barriers, comparison has been made with results obtained by means of variational transition state theory (VTST) [70–72]. The fall-off behavior of canonical kinetic rate constants from the TST limit ($P \rightarrow \infty$) towards the low-pressure limit ($P \rightarrow 0$) has been also studied using statistical RRKM theory [47,73,74]. [TO DELETE:

With this theory, energy-dependent microcanonical rate constants $k(E)$ are first obtained as follows [73]:

$$k(E) = \frac{\sigma N^{\dagger}(E)}{h\rho(E)} \tag{7}$$

where $N^{\dagger}(E)$ denotes the ro-vibrational sum of states at the transition state, and where $\rho(E)$ represents the (RRHO) density of states of reactants. Canonical RRKM rate constants $k(T)$ are then ultimately determined by state integration and Boltzmann averaging:

$$k(T) = \int_{E_o}^{\infty} f(E,T)\, k(E)\, dE \tag{8}$$

along with:

$$f(E,T) = \frac{1}{Q(T)} \rho(E) \exp(-\beta E) \tag{9}$$

where $\beta = 1/k_B T$ and $Q(T)$ is the reactant partition function:

$$Q(T) = \int_{o}^{\infty} \rho(E) \exp(-\beta E)\, dE \tag{10}$$

In the present work, all supplied TST, VTST and RRKM rate constants are the results of chemical kinetic calculations that were performed by means of the Kinetic and Statistical Thermodynamical Package (KiSThelP) by Canneaux *et al.* [75] All these calculations rely upon UM06-2*x*/aug-cc-pVTZ estimations of activation energies and ro-vibrational densities of states. The rationale behind choosing the UM06-2*x* exchange-correlation functional is that a recent study by Zhao and Truhlar [50] has shown that it is the best one for applications involving main-group thermochemistry, kinetics, noncovalent interactions, and electronic excitation energies to valence and Rydberg states. In the RRKM calculations, a scaling factor of 0.971 was imposed on the UM06-2*x*/aug-cc-pVTZ frequencies. Lennard–Jones collision rate theory was used to evaluate collisional stabilization rate constants [76]. The strong collision approximation was assumed to prevail for these calculations, considering therefore that every collision deactivates the activated complex with $\omega = \beta_c . Z_{LJ} . [M]$ being the effective collision frequency, where β_c is the collisional efficiency, Z_{LJ} is the Lennard–Jones collision frequency and [M] is the total gas concentration. The retained value for β_c is 0.2. The collision frequencies (Z_{LJ}) were calculated using the Lennard-Jones parameters: ε/k_B, which depends on the energy depth (ε) of the Lennard-Jones potential, and σ, which measures the extent of the molecular radius [77]. The

retained Lennard-Jones potential parameters for argon as diluent gas amount to σ = 3.465 Å and ε/k_B = 113.5 K [78]. For the thiophene-OH adduct $[C_4H_4S\text{-}OH]^\bullet$, the following parameters have been used: σ = 3.493 Å and ε/k_B = 179.2 K [79].

Canonical VTST [80–89] including Wigner's tunneling corrections has been used mainly for the sake of validating the RRKM approach at a pressure of 1 bar. Indeed, when studying reaction mechanisms involving shallow energy wells and loose transition states, VTST is most commonly regarded as the most reliable approach for estimating kinetic rate coefficients with an accuracy approaching the limits of the assumptions inherent in transition state theory [90–95]. [TO DELETE: A central aspect of the VTST approach involves an assumed separation between the conserved modes, which correspond to vibrations of the separated molecules, and the remaining modes, referred to as the transitional modes, which gradually transform their character throughout the transition state region as the rotations of the separated reactants couple together to form bending and torsional vibrations, and overall rotations in the adduct [96].] With VTST the position of the transition state is varied until the maximum value of the Gibbs free activation energy ($\Delta G^\dagger$) is found for reactions in the gas phase and at gas surface interfaces [83,86,88,89,97], which is equivalent to identifying the dynamical bottleneck where the kinetic rate constant is a minimum [98]. [TO DELETE: This procedure is consistent with the consideration that, since re-crossings of molecular dynamical trajectories from the products to the reactants regions are not accounted for at the level of the critical surface separating these two regions in phase space, RRKM rate constants (and thus TST rate constants in the high-pressure limit) represent upper bounds to the exact kinetic rate constants. The variational TST procedure minimizes thus the re-crossing effects at the dividing critical surface, and gives therefore much more accurate results for rate constants, which can be regarded as benchmark results in the high-pressure limit.] The VTST expression for the rate constant is of the form [98]:

$$k^{\mathrm{GT}}(T,\sigma) = \frac{k_B T}{h} K^{\circ} \exp\left(-\frac{\Delta G^{\mathrm{GT}}(T,\sigma)}{k_B T}\right) \tag{11}$$

where σ represents a collection of parameters defining the dividing surface between the reactants and products, K° defines the standard state, which we choose as 1 cm^3 $molecule^{-1}$, and $\Delta G^{\mathrm{GT}}(T,\sigma)$ is the generalized transition state free activation energy, which is given by:

$$\Delta G^{\mathrm{GT}}(T,\sigma) = \mathrm{V}_{\mathrm{MEP}}(\sigma) - k_{\mathrm{B}}T \ln\left(\frac{Q^{\mathrm{GT}}(T,\sigma)}{K^{\mathrm{o}}\Phi^{\mathrm{R}}(T)}\right) \quad (12)$$

In the above equation, $V_{\mathrm{MEP}}(\sigma)$ is the potential along the reaction coordinate, $Q^{\mathrm{GT}}(T,\sigma)$ is the generalized transition state partition function, and $\Phi^{\mathrm{R}}(T)$ is the reactant partition function per unit volume. In the present work, VTST calculations have been performed in conjunction with a detailed exploration of the IRC path at the UM06-2*x*/aug-cc-pVTZ level. 10 points on both the forward and reverse IRCs have been retained in these computations, using a step size of 0.1 Bohr.

3. Result and discussions

3.1. Energetic and thermodynamic parameters

Since the $[C_4H_4S\text{-}OH]^{\bullet}$ (R1) radical has several resonant structures, the addition of triplet molecular ($^3\sum_g$) oxygen to the $[C_4H_4S\text{-}OH]^{\bullet}$ (R1) radical can occur from *syn* and *anti*-directions at three different positions, namely onto the C_3, C_4, and C_5-atoms, yielding 6 isomers referred to as the so-called R1-*i*OO-*anti*/*syn* (*i* = 3–5) peroxy radicals, respectively (Fig. 1).

The R1-3OO and R1-5OO *syn*/*anti* radicals are found to be by far the most stable structures, compared with the R1-4OO-*syn*/*anti* species. More specifically, all DFT calculations most clearly show that, at room temperature, the O_2 addition reactions onto the C_3 and C_5 positions are strongly exothermic processes ($\Delta H_r < -15$ kcal mol^{-1}), and this both for the *syn* and *anti* addition modes, whereas formation of the R1-4OO-*anti*/*syn* peroxy radicals are strongly endothermic, with reaction enthalpies ranging from 37.6 to 38.9 kcal mol^{-1} (Table 1). The corresponding energy barriers are also much higher (Fig. 1, Table 2). Hence, the formation of these radicals will be negligible under atmospheric conditions. In the sequel, we shall therefore concentrate on the four lowest chemical pathways, corresponding to O_2 addition processes in *syn* and *anti* modes at the C_3 and C_5 positions. In other words, we shall focus on the formation of the R1-*i*OO-*anti*/*syn* (*i*=3,5) radicals, yielding the **P1**–**P4** products (Fig. 1). For the ease of notations, the corresponding chemical pathways will be correspondingly referred to as reaction pathways **1**–**4**, in the section on kinetic parameters.

Table 1. Reaction energies, reaction enthalpies and Gibb's free reaction energies (in kcal mol^{-1}) for the addition of triplet molecular O_2 on the $[C_4H_4S\text{-}OH]^\bullet$ radical, at different levels of theory.

Method / Species	ωB97XD/aug-cc-pVTZ			UM06-2*x*/aug-cc-pVTZ		
	ΔE_{0K}	$\Delta H°_{298K}$	$\Delta G°_{298K}$	ΔE_{0K}	$\Delta H°_{298K}$	$\Delta G°_{298K}$
R1 + O_2	0.000	0.000	0.000	0.000	0.000	0.000
IM-*i*OO-*syn* (*i* = 3,5)	-3.259	-3.071	5.085	-4.981	-5.008	4.283
R1-3OO-*syn*	-9.644	-10.724	1.122	-14.980	-16.072	-4.151
R1-4OO-*syn*	38.832	37.577	47.703	37.999	37.577	47.703
R1-5OO-*syn*	-12.789	-13.852	-1.994	-17.383	-18.527	-6.396
IM-*i*OO-*anti* (*i* = 3,5)	8.290	8.525	16.398	-4.768	-4.688	4.154
R1-3OO-*anti*	-10.576	-11.463	-0.149	-15.430	-16.345	-4.899
R1-4OO-*anti*	39.293	38.860	49.178	38.601	38.147	48.403
R1-5OO-*anti*	-10.427	-11.364	0.068	-14.935	-15.923	-4.339

Table 2. Activation energies, enthalpies and Gibb's free activation energies (in kcal mol^{-1}) for the addition of triplet molecular O_2 on the $[C_4H_4S\text{-}OH]^\bullet$ radical, at different levels of theory.

Method / Species	ωB97XD/aug-cc-pVTZ			UM06-2*x*/aug-cc-pVTZ		
	$\Delta E_{0K}^{\dagger}$	$\Delta H°_{298K}^{\dagger}$	$\Delta G°_{298K}^{\dagger}$	$\Delta E_{0K}^{\dagger}$	$\Delta H°_{298K}^{\dagger}$	$\Delta G°_{298K}^{\dagger}$
R1 + O_2	0.000	0.000	0.000	0.000	0.000	0.000
TS-3OO-*syn*	5.988	5.188	16.193	5.039	4.271	15.225
TS-4OO-*syn*	37.23	36.11	48.20	39.12	38.18	49.72
TS-5OO-*syn*	0.066	-0.754	10.442	-1.773	-2.641	8.782
TS-3OO-*anti*	3.874	3.144	13.977	3.206	2.497	13.188
TS-4OO-*anti*	41.832	40.886	52.456	39.556	38.559	13.188
TS-5OO-*anti*	2.121	1.422	12.120	0.589	-0.214	10.959

All DFT calculations demonstrate that, among all produced isomers, the most stable one is the R1-5OO-*syn* species (Table 1). The reaction energy (ΔE_{0K}) characterizing the formation of the R1-5OO-*syn* radical is all in all lower by about 2.36–2.45 kcal mol^{-1} than the reaction energy for the formation of the R1-5OO-*anti* peroxy radical. On the contrary, the reaction energy characterizing the formation of the R1-3OO-*syn* radical is overall higher by about 0.45–0.93 kcal mol^{-1} than the reaction energy for the formation of the R1-3OO-*anti* peroxy radicals. This stabilization energy for the formation of the R1-5OO-*syn* peroxy radical compared with the R1-5OO-*anti* peroxy radical is in line with the energy which is usually associated with the formation of hydrogen bond. This stabilization energy finds also it origin into an electrostatic interaction between a positively charged hydrogen atom (H_7) and a negatively charged oxygen atom (O_9) − see further section on structural analysis. We note that this observation is similar

to that made in a recent theoretical study of the reaction mechanisms of O_2 addition upon naphthalene–OH adducts, yielding $[C_{10}H_8OH]^{\bullet}$–O_2 peroxy radicals [38]. The formation of hydrogen bonds was also invoked to unravel the atmospheric photo-oxidation mechanisms of toluene [99], an aromatic compound for which the formation of radical structures resulting from the addition of the peroxy and hydroxyl substituents on the same side of the ring scaffold was similarly found to be energetically more favorable.

The activation energy for the formation of the R1-5OO-*syn* radical is lower than that for the formation of the R1-3OO-*syn* radical. Because of some extra-stabilization due to the formation of an intramolecular hydrogen bond between the terminal oxygen of the peroxy group (O_9) and the hydrogen atom of the hydroxyl group (H_7), the barrier heights ($\Delta E_{0K}^{\dagger}$) for the O_2 addition processes from the *syn*-direction are lower than those for the *anti*-mode, by about 1.82 to 2.36 kcal mol^{-1} (Table 2). Similar observations can be made when Gibb's free activation energies are considered: in spite of slightly unfavorable entropy effects, the Gibb's free energy for the *syn* addition mode in C_5 position (8.78–10.44 kcal mol^{-1}) is lower than the ones for the *anti* mode (10.96–12.12 kcal mol^{-1}). O_2 addition at the C_5 position in *syn* mode will thus be both thermodynamically and kinetically favored over O_2 addition in *anti* position. Among all possible adducts, the formation of the R1-5OO-*syn* isomer will clearly therefore predominate under thermodynamic control, i.e. at chemical equilibrium. Both for the *syn* and *anti* modes, O_2 addition in C_5 position is thermodynamically favored over O_2 addition in C_3 position. We note that DFT calculations predict large differences in the relative energies of the identified stationary points, especially with regards to the extent of activation energies. We find nevertheless that the UM06-2*x*/aug-cc-pVTZ activation energies *systematically* underestimate the ωB97XD/aug-cc-pVTZ ones by 0.67 to 1.84 kcal mol^{-1}. Therefore, if rather large differences are to be expected in absolute values from one DFT model to the other for kinetic rate constants, the ultimately obtained branching ratios will nevertheless exhibit a rather limited dependence upon the employed exchange-correlation functionals.

3.2. Structural characteristics of stationary points

The optimized geometries of all identified stationary points involved in the chemical pathways for O_2 addition from the *syn*-direction onto the C_3 and C_5 atoms of the $[C_4H_4S\text{-}OH]^{\bullet}$

energized adduct are supplied at the ωB97XD/aug-cc-pVTZ and UM06-2x/aug-cc-pVTZ levels of theory in Tables 3 and 4, respectively. The reader is correspondingly referred to Fig. 2 for detailed atom labelling. Upon examining this Figure, it appears that the structures describing the R1-3OO-*anti* and R1-5OO-*anti* isomers do not allow the formation of an intramolecular hydrogen bond between the hydroxyl (OH) and peroxy (O_2) substituents. This is in sharp contrast with the observations that can be made for the R1-3OO-*syn* and R1-5OO-*syn* peroxy radical species. Whatever the employed exchange-correlation functional, NBO calculations deliver charges around +0.48 and −0.18 for H_7 and O_9, respectively. These atoms exhibit interdistances in the range 2.16–2.17 Å and 2.37–2.49 Å for the R1-3OO-*syn* and R1-5OO-*syn* radicals, respectively, which are compatible with the idea of a hydrogen bond. On the other hand, these interdistances increase to ~4.7 and ~5.2 Å within the R1-3OO-*anti* and R1-5OO-*anti* structures, and become clearly far too large to enable any significant enough stabilizing electrostatic interaction. These structural preferences explain therefore the larger stability, by 2.36–2.45 kcal mol^{-1}, of the R1-5OO-*syn* structure, relative to the *anti* one.

Addition of O_2 onto the C_3 atom within the R1 energized adduct results into a lengthening of the C_2–C_3 and C_3–C_4 bonds next to the site of addition, by ~0.06 Å and ~0.12 Å, respectively (Table 3). This increase in bond lengths obviously reflects the formation of single C–C bonds near the site of the addition, along with a transfer of the π bond electron density to the newly formed C_3–O_8 bond. Similar structural variations are observed for the O_2 addition process in C_5 position (Table 4), namely an increase of the C_4–C_5 and C_5–S_1 bond lengths, by ~0.11 Å and ~0.07 Å, respectively. Furthermore, in comparison with the geometries obtained for the $[C_4H_4S\text{-}OH]^\bullet$ adduct (R1) (Tables 3 and 4), addition of O_2 to the R1 radical results also in a shortening of the C_2–O_6 bond. Also in line with the formation of an intramolecular hydrogen bond, the O_8–O_9 bond length increases from 1.19–1.20 Å to 1.29–1.30 Å, when the molecular structure evolves from the R1 energized adduct to the R1-3OO-*syn* and R1-5OO-*syn* peroxy radicals. The transition states for O_2 addition at the C_3 and C_5-positions in the R1 energized adduct involve a six-membered cyclic structure [C_2–O_6–H_7–O_9–O_8–C_i (i=3,5)] in which the O_8, O_9 and C_i (i = 3,5) atoms are not co-linear. Indeed, the corresponding bond angles are around 112°–113° (Tables 3 and 4). Like the corresponding energy minima (Fig. 2), these transition state structures are also stabilized by an intramolecular hydrogen bond (H_7–O_9). The hydrogen bond lengths within the

TS-3OO-*syn* and TS-5OO-*syn* structures amount to 1.89–1.93 Å and 2.23–2.26 Å, respectively. It can also be noticed that in the transition states involved in the formation of the R1-3OO-*syn* and R1-5OO-*syn* radical species, the forming C_3–O_8 and C_5–O_8 bond lengths are significantly much longer than in the related products, by 47.9–48.3 % and 47.5–48.2 %, respectively.

Table 3. Structural parameters for all the stationary points that are involved in the R1+O_2→R1-3OO-*syn* reaction pathway (see Fig. 2 for detailed atom labelling).

Parameter \ Method	ωB97XD/aug-cc-pVTZ				UM06-2*x*/aug-cc-pVTZ			
	R	IM	TS	P	R	IM	TS	P
r (S_1–C_2)	1.862	1.866	1.881	1.860	1.857	1.864	1.874	1.854
r (C_2–C_3)	1.493	1.497	1.499	1.557	1.493	1.497	1.496	1.551
r (C_3–C_4)	1.365	1.364	1.399	1.488	1.365	1.362	1.400	1.490
r (C_4–C_5)	1.391	1.393	1.365	1.328	1.393	1.397	1.366	1.330
r (C_5–S_1)	1.729	1.726	1.723	1.743	1.727	1.720	1.723	1.745
r (C_2–O_6)	1.405	1.397	1.373	1.378	1.407	1.396	1.376	1.382
r (O_6–H_7)	0.959	0.961	0.966	0.963	0.961	0.964	0.967	0.965
r (H_7–O_9)	-	2.383	1.894	2.156	-	2.308	1.928	2.170
r (C_3–O_8)	-	3.407	2.169	1.463	-	3.234	2.157	1.458
r (O_8–O_9)	1.196	1.198	1.238	1.301	1.190	1.194	1.231	1.298
θ(C_2–O_6–H_7)	109.35	108.07	109.64	108.67	109.49	107.99	109.86	108.83
θ(C_3–O_8–O_9)	-	94.45	117.62	112.54	-	95.08	118.51	111.98

- Bond lengths are in angstrom (Å) and torsion and dihedral angles are in degrees (°)

Table 4. Structural parameters for all the stationary points that are involved in the R1+O_2→R1-5OO-*syn* reaction pathway (see Fig. 2 for detailed atom labelling).

Parameter \ Method	ωB97XD/aug-cc-pVTZ				UM06-2*x*/aug-cc-pVTZ			
	R	IM2	TS	P	R	IM	TS	P
r (S_1–C_2)	1.862	1.866	1.865	1.846	1.857	1.864	1.860	1.842
r (C_2–C_3)	1.493	1.497	1.499	1.504	1.493	1.497	1.500	1.506
r (C_3–C_4)	1.365	1.364	1.341	1.320	1.365	1.362	1.342	1.320
r (C_4–C_5)	1.391	1.393	1.424	1.495	1.393	1.397	1.342	1.498
r (C_5–S_1)	1.729	1.726	1.714	1.795	1.727	1.720	1.426	1.797
r (C_2–O_6)	1.405	1.397	1.388	1.393	1.407	1.396	1.711	1.395
r (O_6–H_7)	0.959	0.961	0.965	0.964	0.961	0.964	0.967	0.967
r (H_7–O_9)	-	2.383	2.264	2.486	-	2.308	2.231	2.367
r (C_5–O_8)	-	3.053	2.192	1.479	-	2.813	2.174	1.474
r (O_8–O_9)	1.196	1.198	1.228	1.295	1.190	1.194	1.223	1.292
θ(C_2–O_6–H_7)	109.35	108.07	107.09	107.45	109.49	107.99	107.30	107.25
θ(C_5–O_8–O_9)	-	101.30	108.12	112.94	-	100.12	107.07	112.65

- Bond lengths are in angstrom (Å) and torsion and dihedral angles are in degrees (°)

For the sake of completeness and clarity, it is worth noticing that the IM1 and IM3 intermediates on pathways **1** and **3** (O_2 additions from the *syn*-direction in C_3 or C_5 positions) are structurally almost the same and exhibit practically equal energies, to such an extent that these energies cannot be distinguished on the scale of Fig. 1. Similarly, the IM2 and IM4 intermediates on pathways **2** and **4** (O_2 additions from the *anti*-direction in C_3 or C_5 positions) have almost the same structures, with almost equal energies.

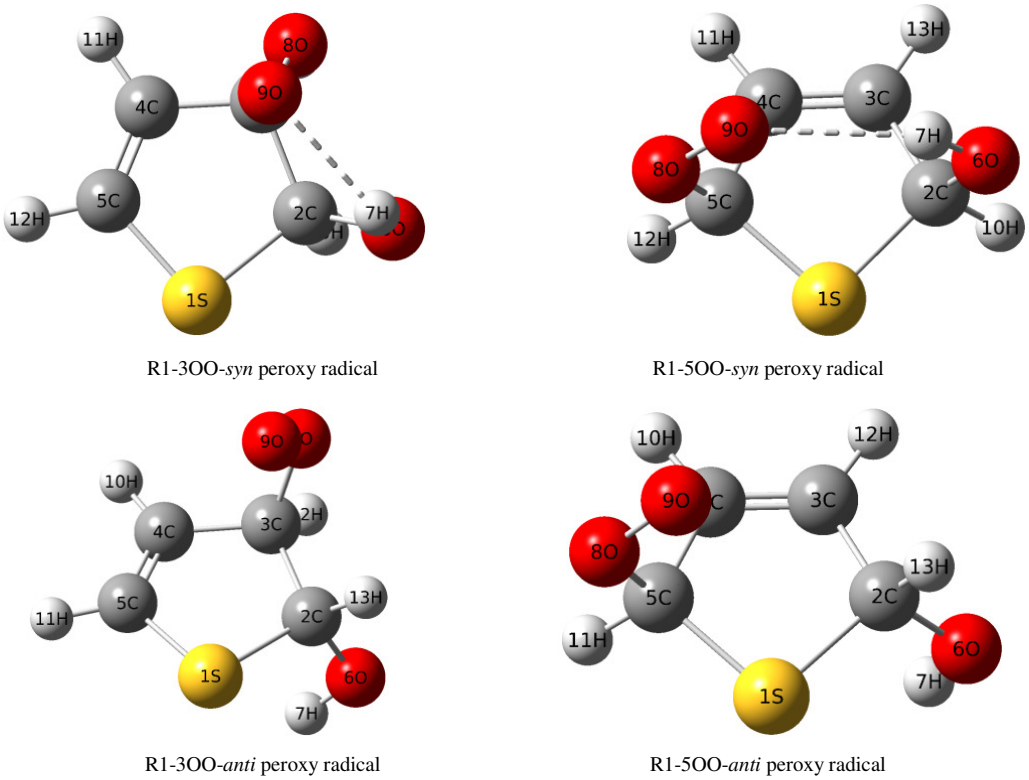

Fig. 2. Optimized geometries of the R1-3OO and R1-5OO peroxy radicals.

Hammond's postulate states that the structure of a transition state resembles that of the species nearest to it in free energy. This principle is usually quantified in terms of the position of the transition structure along the reaction coordinate, n_T, as defined by Agmon [100]:

$$n_T = \frac{1}{2-(\Delta G/\Delta G^{\dagger})} \tag{13}$$

The magnitude of n_T, indicates the degree of similarity between the transition structure and the product. According to the above equation, the position of the transition state along the reaction

coordinate is determined solely by the Gibb's free reaction energy, ΔG, and the Gibb's free activation energy, $\Delta G^{\dagger}$.

Table 5. Analysis of the chemical pathways of interest in terms of n_T values.

Pathway \ Method	ωB97XD/aug-cc-pVTZ	UM06-2*x*/aug-cc-pVTZ
R1+O_2 → R1-3OO-*syn*	0.5179	0.4401
R1+O_2 → R1-5OO-*syn*	0.4564	0.3665
R1+O_2 → R1-3OO-*anti*	0.4974	0.4217
R1+O_2 → R1-5OO-*anti*	0.5014	0.4174

DFT estimates of n_T values for the *syn*-addition of O_2 to the $[C_4H_4S\text{-}OH]^{\bullet}$ radical are supplied in Table 5. In line with the previously obtained energy profiles (Fig. 1), and the structural observations made in the preceding section, the obtained values imply that the transition state involved in the formation of the R1-5OO-*syn* radical is more similar to the reactant than the transition state involved in the formation of the R1-3OO-*syn* radical. The same observation can be made when considering the *anti* mode for O_2 addition onto the $[C_4H_4S\text{-}OH]^{\bullet}$ radical.

3.3. Natural bond orbital analysis

Delocalization of electron density among the filled (bonding or lone pair) Lewis type NBOs and the empty (antibonding and Rydberg) non-Lewis NBOs results into a transfer of occupancy from the localized NBOs of the idealized Lewis structure into the empty non-Lewis orbitals, resulting into a significant departure from an idealized Lewis structure description. This transfer is referred to as a "delocalization" correction to the zero-order natural Lewis structure, which relates to a stabilizing donor-acceptor interaction, the extent of which can be estimated by means of second-order perturbation theory [56]. Indeed, for each donor NBO(i) and acceptor NBO(j), the stabilization energy (E_2) associated with the $i \rightarrow j$ delocalization can be estimated as follows [101]:

$$E_2 = \Delta E_{ij} = q_i \left(\frac{F_{(i,j)}^2}{\varepsilon_i - \varepsilon_j} \right) \tag{14}$$

where q_i is the donor orbital occupancy, ε_i and ε_j are diagonal elements (orbital energies) of the NBO Fock matrix, and $F_{(i,j)}$ are off-diagonal elements of this matrix.

In line with the formation of intramolecular hydrogen bonds between the hydroxyl and peroxy substituents, more specifically between the H_7 and O_9 atoms, the NBO analysis of donor–acceptor interactions (Table 6) shows that, for both the R1-3OO-*syn* and R1-5OO-*syn* isomers, rather significant stabilization energies (E_2) are associated with electron delocalization from the non-bonding lone-pair in the peroxy substituent [$n(O_9)$] to the $\sigma^*_{O6–H7}$ antibonding orbital in the hydroxyl substituent. As was noted for the hydroxycyclohexadienyl peroxy radical, hyperconjugative interactions lead also to an increase in the population of the $\sigma^*_{O6–H7}$ antibonding orbital, which weakens in turn the O_6–H_7 bond.

Table 6. NBO occupancies and delocalization energies (E_2) (in kcal mol^{-1}) characterizing at different DFT levels the R1-3OO-*syn* (**1**) and R1-5OO-*syn* (**2**) peroxy radicals (results obtained using the aug-cc-pVTZ basis set).

	ωB97XD/aug-cc-pVTZ		UM06-2*x*/aug-cc-pVTZ	
	(**1**)	(**2**)	(**1**)	(**2**)
Occupancies				
$\sigma(O_6–H_7)$	0.99226	0.99414	0.99259	0.99416
$\sigma^*(O_6–H_7)$	0.00707	0.00617	0.00675	0.00669
$n(O_9)$	0.99617	0.97788	0.99643	0.97891
Delocalization energies (E_2)				
$n(O_9)\rightarrow\sigma^*(O_6–H_7)$	0.29	0.34	< 0.25	0.41

More specifically, the NBO results indicate that for the R1-5OO-*syn* isomer, delocalization of the oxygen lone pair of the O_9 atom [$n(O_9)$] onto the H_7 atom results in a net stabilization, in the energy range 0.34–0.41 kcal mol^{-1}. Besides, hyperconjugative $n(O_9)\rightarrow\sigma^*_{O6–H7}$ interactions for the R1-3OO-*syn* radical result in a stabilization by less than 0.3 kcal mol^{-1}. Besides, increase of the extent of delocalization of the $n(O_9)$ lone pair onto the $\sigma^*_{O6–H7}$ antibonding orbital from the R1-3OO-*syn* to the R1-5OO-*syn* structures correlates with a decrease of the occupation of one of the non-bonding lone-pair orbitals on the O_9 atom [$n(O_9)$].

3.4. Kinetic parameters

All kinetic rate constants that are supplied in the sequel were obtained according to our best estimates of energy barriers, i.e. using DFT along with the UM06-2*x* exchange-correlation

functional. A two-step mechanism is assumed, involving first a fast and reversible pre-equilibrium between the reactants (R1 and O_2) and a pre-reactive complex $[C_4H_4S\text{-}OH\ldots O_2]^\bullet$ (IM), followed by the irreversible formation of the thiophene peroxy radicals R1-*i*OO-*syn*/*anti* (*i* = 3, 5). Effective rate constants $k_{eff}(\boldsymbol{i})$ [$\boldsymbol{i}$=**1**,**2**,**3**,**4**] for the four lowest chemical pathways (Fig. 1) leading to products **P1**-**P4** were obtained correspondingly according to a steady-state analysis. With our notation, **1** and **2** denote the formation of the R1-3OO-*syn*/*anti* radicals, whereas **3** and **4** denote the formation of the R1-5OO-*syn*/*anti* radicals, respectively.

Whatever the considered temperatures, the effective rate constant for the formation of the R1-5OO-*syn* radical is larger than that obtained for the R1-3OO-*syn* radical, which is in line with a reduction of the activation energy barrier, by ~6.8 kcal mol^{-1} (UM06-2*x*/aug-cc-pVTZ estimate), on the corresponding chemical reaction pathways. Indeed, the supplied TST, VTST, and RRKM results (Tables 7–9) obtained along with the UM06-2*x*/aug-cc-pVTZ approach indicate that the unimolecular kinetic rate constants k_2(**3**) which were obtained for the IM1→R1-5OO-*syn* reaction step are larger by factors ranging from ~37 to 4.9×10^4 than the rate constants, k_2(**1**) that were obtained for the IM1→R1-3OO-*syn* unimolecular reaction step. At a pressure of 1 bar, the formation of the R1-5OO-*syn* species will therefore clearly predominate over the formation of the R1-3OO-*syn* species. The same observation holds for all considered temperatures (from 298 to 471 K) and for pressures ranging from 10^{-10} to 10^4 bars (see Tables S1a–S1r in the Supporting Information). As is to be expected, because of the involved positive energy barriers, these rate constants gradually increase when the temperature increases. Rather unsurprisingly, since the equilibrium constants for the first reversible reaction step ($K_c = K_p/RT$) do not depend very much on the site of addition (see data supplied in Tables S2a–S2h in the Supporting Information), this results in turn into a larger effective rate constant, by about one order of magnitude, for addition of O_2 in *syn* mode and in C_5 position, compared with the effective rate constants obtained for O_2 addition in *syn* mode and in C_3 position.

Similar observations can be made for the *anti* modes of addition. Here also, in line with lower activation energies (by ~2.6 kcal mol^{-1} as well), rate constants k_2(**4**) for the IM4→R1-5OO-*anti* unimolecular rearrangement reaction step are larger by factors ranging from about 3.5 to 36.7, than the rate constants k_2(**2**) obtained for the IM2→R1-3OO-*anti* unimolecular reaction step. At a pressure of 1 bar, the formation of the R1-5OO-*anti* species will therefore clearly predominate over the formation of the R1-3OO-*anti* species, whatever the considered temperatures and

pressures (see Tables S1a–S1r in the Supporting Information). Again, since the equilibrium constants for the first reversible reaction do not depend very much on the site of addition (see data supplied in Tables S2a–S2h in the Supporting Information), this results in turn into a larger effective rate constant, by about one order of magnitude, for addition of O_2 in *anti* mode and in C_5 position, compared with the effective rate constants obtained for O_2 addition in *anti* mode and in C_3 position. Thus, whatever the addition (*syn* or *anti*) mode, O_2 addition in C_5 position is not only thermodynamically but also kinetically favored over O_2 addition in C_3 position. Since the involved energy barriers are significantly larger, by 1.8 to 2.4 kcal mol^{-1}, the formation of the R1-3OO-*anti* and R1-5OO-*anti* species is characterized by significantly lower rate constants at temperatures ranging from 298 to 471 K, by one to two orders of magnitude, compared with the formation of the R1-3OO-*syn* and R1-5OO-*syn* isomers (Tables 7–9).

Table 7. Unimolecular rate constants (in s^{-1}), and effective bimolecular rate constants (in cm^3 $molecule^{-1}$ s^{-1}) for the reported reaction channels obtained by means of TST theory ($P = 1$ bar), according to the computed UM06-2*x*/aug-cc-pVTZ energy profiles (*x*=1 or 3, *y*=2 or 4).

T	Rate constant						Effective rate constant (cm^3 $molecule^{-1}$ s^{-1})			
	anti mode			*syn* mode			*anti* mode		*syn* mode	
(K)	IM*x*→R1+O_2 (k_{-1})	IM2→R1-3OO k_2(**2**)	IM4→R1-5OO k_2(**4**)	IM*y*→R1+O_2 (k_{-1})	IM1→R1-3OO k_2(**1**)	IM3→R1-5OO k_2(**3**)	R1+O_2→R1-3OO [k_{eff}(**2**)]	R1+O_2→R1-5OO [k_{eff}(**4**)]	R1+O_2→R1-3OO [k_{eff}(**1**)]	R1+O_2→R1-5OO [k_{eff}(**3**)]
298	6.91×10^{15}	8.82×10^{5}	1.97×10^{7}	8.59×10^{15}	5.41×10^{4}	1.38×10^{9}	7.70×10^{-18}	1.72×10^{-16}	2.63×10^{-19}	6.70×10^{-15}
322	4.43×10^{15}	2.40×10^{6}	4.01×10^{7}	5.42×10^{15}	1.86×10^{5}	2.10×10^{9}	1.41×10^{-17}	2.35×10^{-16}	6.00×10^{-19}	6.78×10^{-15}
353	2.74×10^{15}	7.15×10^{6}	8.67×10^{7}	3.30×10^{15}	7.15×10^{5}	3.32×10^{9}	2.80×10^{-17}	3.39×10^{-16}	1.51×10^{-18}	7.01×10^{-15}
380	1.94×10^{15}	1.60×10^{7}	1.53×10^{8}	2.30×10^{15}	1.93×10^{6}	4.65×10^{9}	4.69×10^{-17}	4.48×10^{-16}	3.02×10^{-18}	7.27×10^{-15}
400	1.55×10^{15}	2.70×10^{7}	2.22×10^{8}	1.82×10^{15}	3.69×10^{6}	5.78×10^{9}	6.59×10^{-17}	5.42×10^{-16}	4.77×10^{-18}	7.47×10^{-15}
425	1.21×10^{15}	4.86×10^{7}	3.35×10^{8}	1.41×10^{15}	7.62×10^{6}	7.38×10^{9}	9.76×10^{-17}	6.72×10^{-16}	8.05×10^{-18}	7.80×10^{-15}
442	1.04×10^{15}	6.97×10^{7}	4.33×10^{8}	1.21×10^{15}	1.19×10^{7}	8.57×10^{9}	1.25×10^{-16}	7.74×10^{-16}	1.11×10^{-17}	8.00×10^{-15}
457	9.23×10^{14}	9.36×10^{7}	5.33×10^{8}	1.06×10^{15}	1.71×10^{7}	9.68×10^{9}	1.53×10^{-16}	8.71×10^{-16}	1.45×10^{-17}	8.19×10^{-15}
471	8.30×10^{14}	1.21×10^{8}	6.39×10^{8}	9.53×10^{14}	2.36×10^{7}	1.08×10^{10}	1.83×10^{-16}	9.64×10^{-16}	1.84×10^{-17}	8.43×10^{-15}

Table 8. Unimolecular rate constants (in s^{-1}), and effective bimolecular rate constants (in cm^3 $molecule^{-1}$ s^{-1}) for the reported reaction channels obtained by means of VTST theory ($P = 1$ bar), according to the computed UM06-2*x*/aug-cc-pVTZ energy profiles (*x*=1 or 3, *y*=2 or 4).

T	Rate constant						Effective rate constant (cm^3 $molecule^{-1}$ s^{-1})			
	anti mode			*syn* mode			*anti* mode		*syn* mode	
(K)	IM*x*→R1+O_2 (k_{-1})	IM2→R1-3OO k_2(**2**)	IM4→R1-5OO k_2(**4**)	IM*y*→R1+O_2 (k_{-1})	IM1→R1-3OO k_2(**1**)	IM3→R1-5OO k_2(**3**)	R1+O_2→R1-3OO [k_{eff}(**2**)]	R1+O_2→R1-5OO [k_{eff}(**4**)]	R1+O_2→R1-3OO [k_{eff}(**1**)]	R1+O_2→R1-5OO [k_{eff}(**3**)]
298	6.91×10^{15}	6.94×10^{4}	2.55×10^{6}	8.59×10^{15}	4.94×10^{3}	2.41×10^{8}	6.06×10^{-19}	2.23×10^{-17}	2.40×10^{-20}	1.17×10^{-15}
322	4.43×10^{15}	2.00×10^{5}	5.46×10^{6}	5.42×10^{15}	1.79×10^{4}	3.85×10^{8}	1.17×10^{-18}	3.21×10^{-17}	5.79×10^{-20}	1.24×10^{-15}
353	2.74×10^{15}	6.31×10^{5}	1.25×10^{7}	3.30×10^{15}	7.28×10^{4}	6.40×10^{8}	2.47×10^{-18}	4.88×10^{-17}	1.54×10^{-19}	1.35×10^{-15}
380	1.94×10^{15}	1.47×10^{6}	2.29×10^{7}	2.30×10^{15}	2.05×10^{5}	9.29×10^{8}	4.31×10^{-18}	6.71×10^{-17}	3.20×10^{-19}	1.45×10^{-15}
400	1.55×10^{15}	2.55×10^{6}	3.40×10^{7}	1.82×10^{15}	4.01×10^{5}	1.18×10^{9}	6.24×10^{-18}	8.31×10^{-17}	5.19×10^{-19}	1.53×10^{-15}
425	1.21×10^{15}	4.73×10^{6}	5.29×10^{7}	1.41×10^{15}	8.52×10^{5}	1.55×10^{9}	9.49×10^{-18}	1.06×10^{-16}	9.00×10^{-19}	1.64×10^{-15}

442	1.04×10^{15}	6.91×10^{6}	6.94×10^{7}	1.21×10^{15}	1.35×10^{6}	1.83×10^{9}	1.24×10^{-17}	1.24×10^{-16}	1.26×10^{-18}	1.71×10^{-15}
457	9.23×10^{14}	9.42×10^{6}	8.66×10^{7}	1.06×10^{15}	1.98×10^{6}	2.09×10^{9}	1.54×10^{-17}	1.42×10^{-16}	1.67×10^{-18}	1.77×10^{-15}
471	8.30×10^{14}	1.24×10^{7}	1.05×10^{8}	9.53×10^{14}	2.75×10^{6}	2.35×10^{9}	1.87×10^{-17}	1.59×10^{-16}	2.15×10^{-18}	1.84×10^{-15}

Table 9. Unimolecular rate constants (in s^{-1}), and effective bimolecular rate constants (in cm^3 $molecule^{-1}$ s^{-1}) for the reported reaction channels obtained by means of RRKM theory (P = 1 bar), according to the computed UM06-2*x*/aug-cc-pVTZ energy profiles (x=1 or 3, y=2 or 4).

T	Rate constant						Effective rate constant (cm^3 $molecule^{-1}$ s^{-1})			
	anti mode			*syn* mode			*anti* mode		*syn* mode	
(K)	IM*x*→R1+O_2 (k_{-1})	IM2→R1-3OO k_2(**2**)	IM4→R1-5OO k_2(**4**)	IM*y*→R1+O_2 (k_{-1})	IM1→R1-3OO k_2(**1**)	IM3→R1-5OO k_2(**3**)	R1+O_2→R1-3OO [k_{eff}(**2**)]	R1+O_2→R1-5OO [k_{eff}(**4**)]	R1+O_2→R1-3OO [k_{eff}(**1**)]	R1+O_2→R1-5OO [k_{eff}(**3**)]
298	6.91×10^{15}	6.86×10^{5}	1.31×10^{7}	8.59×10^{15}	4.70×10^{4}	2.94×10^{8}	5.99×10^{-18}	1.14×10^{-16}	2.28×10^{-19}	1.43×10^{-15}
322	4.43×10^{15}	1.83×10^{6}	2.51×10^{7}	5.42×10^{15}	1.61×10^{5}	3.69×10^{8}	1.07×10^{-17}	1.47×10^{-16}	5.20×10^{-19}	1.19×10^{-15}
353	2.74×10^{15}	5.19×10^{6}	4.90×10^{7}	3.30×10^{15}	6.08×10^{5}	4.53×10^{8}	2.03×10^{-17}	1.92×10^{-16}	1.28×10^{-18}	9.56×10^{-16}
380	1.94×10^{15}	1.09×10^{7}	7.78×10^{7}	2.30×10^{15}	1.59×10^{6}	5.10×10^{8}	3.19×10^{-17}	2.28×10^{-16}	2.49×10^{-18}	7.98×10^{-16}
400	1.55×10^{15}	1.75×10^{7}	1.03×10^{8}	1.82×10^{15}	2.96×10^{6}	5.41×10^{8}	4.27×10^{-17}	2.51×10^{-16}	3.83×10^{-18}	6.99×10^{-16}
425	1.21×10^{15}	2.90×10^{7}	1.39×10^{8}	1.41×10^{15}	5.81×10^{6}	5.70×10^{8}	5.82×10^{-17}	2.79×10^{-16}	6.14×10^{-18}	6.02×10^{-16}
442	1.04×10^{15}	3.91×10^{7}	1.65×10^{8}	1.21×10^{15}	8.73×10^{6}	5.83×10^{8}	6.99×10^{-17}	2.95×10^{-16}	8.15×10^{-18}	5.44×10^{-16}
457	9.23×10^{14}	4.96×10^{7}	1.88×10^{8}	1.06×10^{15}	1.21×10^{7}	5.90×10^{8}	8.11×10^{-17}	3.07×10^{-16}	1.02×10^{-17}	4.99×10^{-16}
471	8.30×10^{14}	6.08×10^{7}	2.09×10^{8}	9.53×10^{14}	1.60×10^{7}	5.95×10^{8}	9.18×10^{-17}	3.15×10^{-16}	1.25×10^{-17}	4.64×10^{-16}

[TO DELETE ? The reader is referred to Fig. 3 for an Arrhenius plot of the obtained RRKM estimates at a pressure of 1 bar of the effective rate constants for O_2 addition in C_3 and C_5 positions and in the *syn*/*anti* addition modes (pathways **1**–**4**), according to the UM06-2*x*/aug-cc-pVTZ estimates of energy barriers. This Figure clearly confirms that the production of the R1-5OO-*syn* peroxy radical dominates the overall reaction mechanism under atmospheric pressure and at temperatures ranging from 298 to 471 K. The same conclusion holds at much lower pressures, down to 10^{-10} bar (see Tables S2a–S2h of the Supporting Information).]

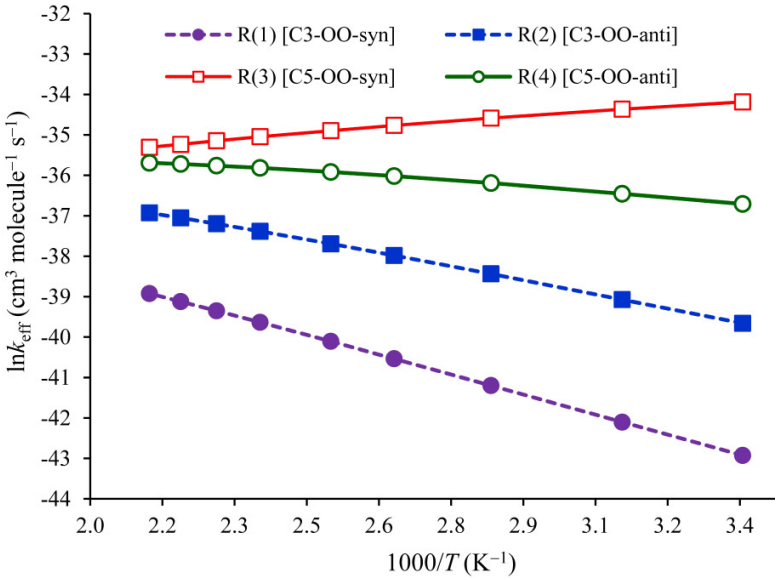

Fig. 3. Arrhenius plot of the obtained RRKM bimolecular rate constants (for R1+O_2→R1-*i*OO-*syn,* with *i*=3,5) using the UM06-2*x*/aug-cc-pVTZ approach. Legend: (●) theoretical rate constant obtained for the R1+O_2→R1-3OO-*syn* pathway; (■) theoretical rate constant obtained for the R1+O_2→R1-3OO-*anti* pathway; (□) theoretical rate constant obtained for the R1+O_2→R1-5OO-*syn* pathway; (○) theoretical rate constant obtained for the R1+O_2→R1-5OO-*anti* pathway.

Consistently with the way these theories were derived (see refs. 40–50 and 70–72), it appears upon a comparison of Tables 7–9 that TST (i.e. RRKM in the high-pressure limit) overestimates the benchmark VTST kinetic rate constants by at most one order of magnitude, which justifies using RRKM theory for studying the fall-off behavior of these rate constants towards the low-pressure limit. We remind indeed that RRKM theory (which reduces to TST in the high-pressure limit) is derived upon an ergodic analysis of molecular dynamical trajectories in phase space and the assumption that energized molecules pass through the transition state only once, an approximation which may not always been exact, hence RRKM rate constants necessarily represent upper bounds to the exact kinetic rate constants.

Branching ratios at a pressure of 1 bar and temperatures ranging from 298 to 471 K are reported for the four retained chemical pathways in Table 10, for the sake of more quantitative insights into the regioselectivity of O_2 addition on the $[C_4H_4S\text{-}OH]^\bullet$ radical. These branching rations were obtained using TST, VTST and RRKM theories, in conjunction with the UM06-2*x*/aug-cc-pVTZ estimates for effective rate constants (equations 15–18). Under these conditions, TST and VTST estimates of branching ratios at a pressure of 1 bar are almost identical. On the

other hand, these branching ratios significantly differ from the RRKM values obtained for a standard pressure of 1 bar, especially at high temperatures, due to the extreme pressure dependence of the global bimolecular kinetic rate constant characterizing pathway **3** (R1+O_2→R1-5OO-*syn*).

$$R(i) = \frac{k_{\text{eff}}(i)}{k_{\text{eff}}(\mathbf{1}) + k_{\text{eff}}(\mathbf{2}) + k_{\text{eff}}(\mathbf{3}) + k_{\text{eff}}(\mathbf{4})}; \quad i=\mathbf{1}-\mathbf{4} \tag{19}$$

Further RRKM estimates of these branching ratios at the same temperatures and at pressures ranging from 10^{-10} to 10^{4} bars are supplied in Tables S2a–S2h of the Supporting Information.

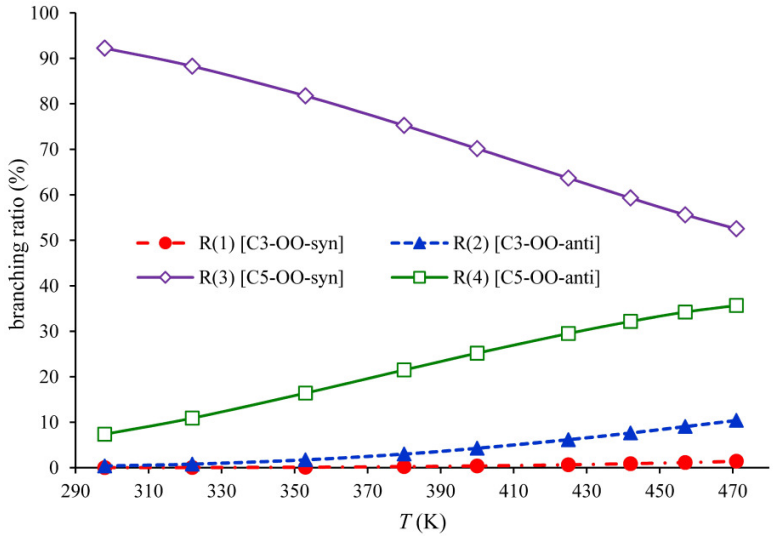

Fig. 4. Evaluation of branching ratios in function of the temperature for pathways R1+O_2→R1-*i*OO-*syn* (*i*=3,5) using the UM06-2*x*/aug-cc-pVTZ approach. Legend: (●) data obtained for the R1+O_2→R1-3OO-*syn* pathway; (▲) data obtained for the R1+O_2→R1-3OO-*anti* pathway; (◇) data obtained for the R1+O_2→R1-5OO-*syn* pathway; (□) data obtained for the R1+O_2→R1-5OO-*anti* pathway.

Upon comparing Tables 7, 8 and 9, it appears overall that kinetic rate constants obtained at a pressure of 1 bar using the TST, VTST and RRKM approaches in conjunction with the same energy profiles do not appreciably differ. The largest discrepancy is found for the rate constant characterizing the second unimolecular reaction step in pathway **3** [k_2(**3**)], and this discrepancy is of the order of a factor 10 only. It is therefore preferable to consider the RRKM approach for evaluating kinetic rate constants, since in this case it is possible to account for the strong dependence of rate constants upon the pressure, at pressures lower than 100 bar (see further). On the other hand, tunneling effects appear to be (almost) negligible. Indeed, based on the computed

UM06-2*x* energy profiles and UM06-2*x*/aug-cc-pVTZ vibrational frequencies, $\kappa(T)$ values ranging from 1.05 to 1.20 were found for TST calculations of the kinetic rate constant (k_2) characterizing the second unimolecular reaction step involved in pathways **1**–**4**, respectively.

Table 10. Branching ratios for the reported reaction channels obtained by means of TST and RRKM theories (P = 1 bar), according to the computed UM06-2*x*/aug-cc-pVTZ energy barriers.

Pathways / T (K)	R1+O_2→R1-3OO-*syn* (**1**)			R1+O_2→R1-3OO-*anti* (**2**)			R1+O_2→R1-5OO-*syn* (**3**)			R1+O_2→R1-5OO-*anti* (**4**)		
	TST	VTST	RRKM	TST	VTST	RRKM	TST	VTST	RRKM	TST	VTST	RRKM
298	0.00	0.00	0.01	0.11	0.05	0.39	97.38	98.08	92.25	2.50	1.87	7.35
322	0.01	0.00	0.04	0.20	0.09	0.79	96.45	97.38	88.26	3.34	2.52	10.90
353	0.02	0.01	0.11	0.38	0.18	1.74	95.01	96.33	81.74	4.59	3.48	16.42
380	0.04	0.02	0.23	0.60	0.28	3.01	93.59	95.29	75.26	5.77	4.41	21.50
400	0.06	0.03	0.38	0.82	0.39	4.28	92.42	94.45	70.14	6.71	5.13	25.19
425	0.09	0.05	0.65	1.14	0.54	6.16	90.93	93.37	63.68	7.83	6.04	29.51
442	0.12	0.07	0.89	1.40	0.67	7.62	89.79	92.55	59.32	8.69	6.71	32.17
457	0.16	0.09	1.14	1.66	0.80	9.04	88.75	91.75	55.61	9.44	7.36	34.21
471	0.19	0.11	1.42	1.91	0.93	10.39	87.85	91.10	52.53	10.05	7.87	35.66

In Figs. 4 and 5, we display the evolution of RRKM branching ratios for the *syn*-addition of O_2 in C_3 and C_5 positions as a function of the temperature and pressure, respectively (see also Table 8 and Table S3a–S3i of the Supporting Information for the corresponding numerical values). These data show that, whatever the addition mode (*syn* or *anti*), the regioselectivity of the reactions with regards to the location of the addition site strongly decreases with increasing temperatures (Fig. 4). Pressures decreasing from 10^0 to 10^{-4} bar results into strong decreases of the regioselectivities, which stabilize to constant values at lower pressures (Fig. 5). In line with the computed energy profile and kinetic rate constants, the formation of the R1-5OO-*syn* isomer (pathway **3**) clearly predominates over the formation of the R1-3OO-*syn* isomer (pathway **1**). In view of the supplied RRKM data (see Tables S2a–S2h of the Supporting Information), it is therefore more than certain that, at all considered temperatures, the production of the R1-5OO-*syn* species dominates the overall reaction mechanism, and this down to extremely low pressures, larger than 10^{-10} bar.

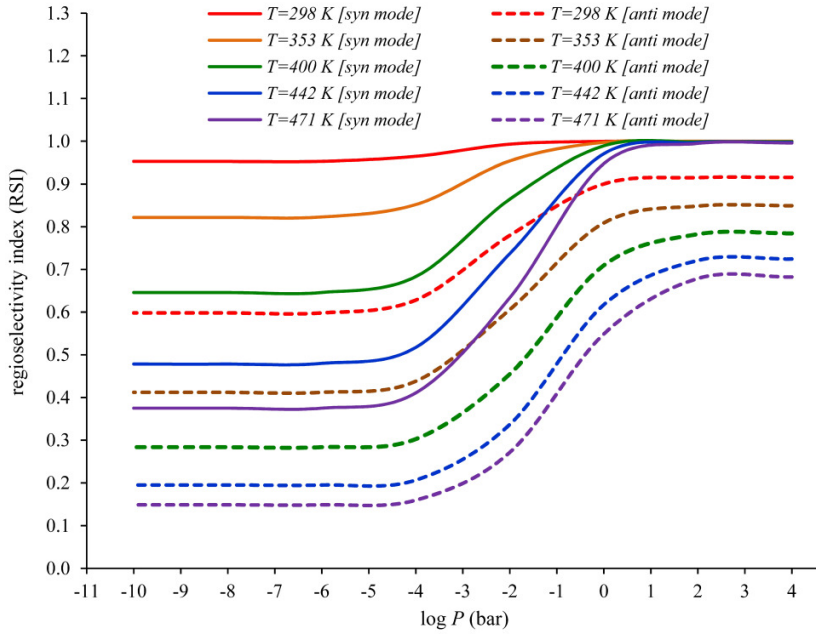

Fig. 5. Dependence upon the pressure and temperature of the regioselectivities [RSI=*R*(**3**)–*R*(**1**)/*R*(**1**)+*R*(**3**)] and [RSI=*R*(**4**)–*R*(**2**)/*R*(**2**)+*R*(**4**)] of O_2 addition in *syn* and *anti* modes onto the thiophene-OH adduct $[C_4H_4S\text{-}OH]^\bullet$, according to the RRKM estimates of effective rate constants [k_{eff}(**1**), k_{eff}(**2**), k_{eff}(**3**), k_{eff}(**4**)] supplied in Tables S3a–S3i (see Supporting Information), based on UM06-2*x*/aug-cc-pVTZ energy profiles.

Upon inspecting Fig. 3 and Table 9, it is clear that the RRKM effective rate constants obtained from the UM06-2*x* energy profiles for the R1+O_2→R1-5OO-*syn* reaction pathways decrease with increasing temperatures whereas for all other investigated reaction pathways, an increase of the global rate constant is observed when the temperature increases. Furthermore, upon inspecting the RRKM data displayed in Fig. 4, it appears quite clearly that, in line with energy barriers larger than 3.2 kcal mol^{-1}, pressures larger than 10 bar are in general sufficient for ensuring a saturation within 10 % accuracy of the computed effective kinetic rate constants compared with the high-pressure limit. In line with our preceding study of the formation of the $[C_{10}H_8OH]^\bullet$ adduct resulting from the addition reactions of hydroxyl radicals onto naphthalene [102], comparison with the RRKM data nevertheless indicates that the TST approximation breaks down at pressures lower than 10^2 bar for the global bimolecular rate constant characterizing pathway **3** [k_{eff}(**3**)] (i.e. R1+O_2→R1-5OO-*syn*), due to the negative activation energy (−1.77 kcal mol^{-1}) characterizing this reaction pathway (Fig. 1). At a pressure of 1 bar, detailed inspection of Tables 7 and 9 shows that ratios between the TST and RRKM estimates

for this rate constant increases from ~4.7 to ~18.2 as the temperature increases from 298 to 471 K.

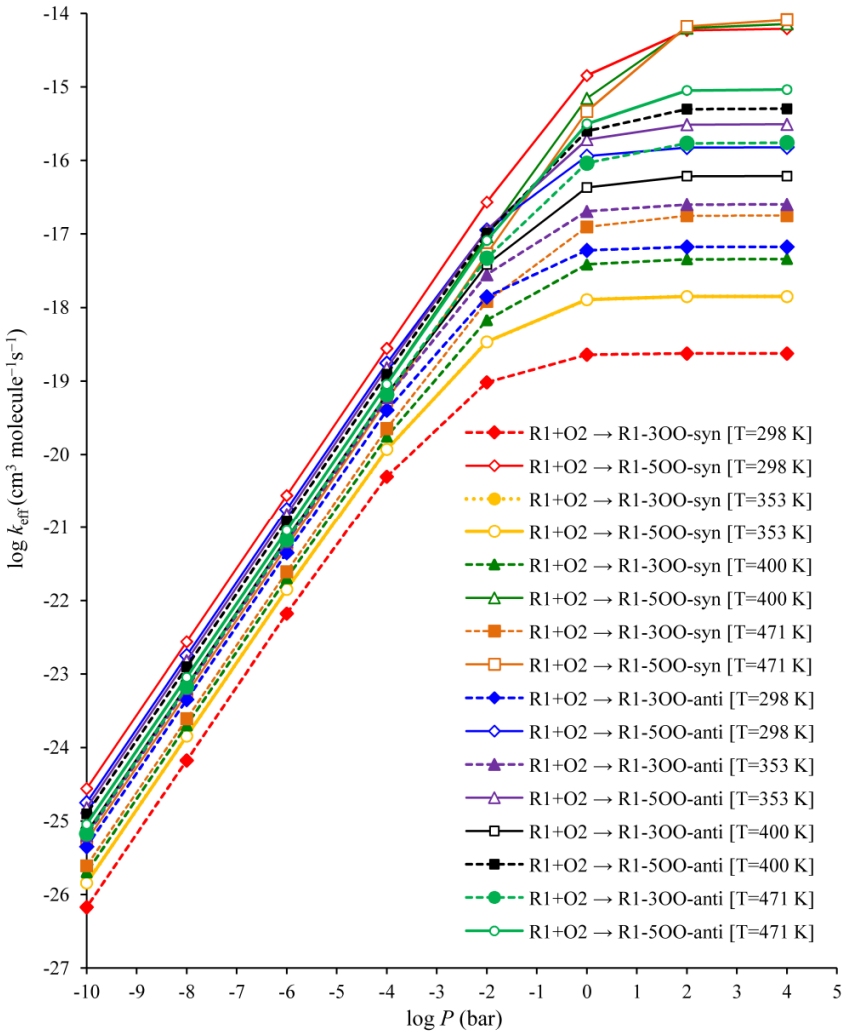

Fig. 6. Pressure dependence of the bimolecular rate constants for the R1+O_2→R1-*i*OO-*syn/anti* (*i* = 3,5) reaction pathways according to the UM06-2*x*/aug-cc-pVTZ energy profiles (RRKM results, obtained by means of equations 15–18).

4. Conclusions

The reaction mechanisms for the atmospheric oxidation of the main (kinetically dominant) thiophene-OH adduct [C_4H_4S-OH]$^\bullet$ (R1) by molecular oxygen in its triplet electronic ground state have been studied computationally using Density Functional Theory along with the *ω*B97XD and UM06-2*x* exchange-correlation functionals and the aug-cc-pVTZ basis set. All our

calculations indicate that, from a thermodynamic viewpoint, the most favorable process is O_2 addition at the C_5 position in *syn* mode.

A combined structural, energetic and natural bond orbital analysis shows that the intramolecular H-bond in the R1-5OO-*syn* radical is stronger than that in the R1-3OO-*syn* radical. Analysis of the computed structures, bond orders and free energy profiles demonstrates that all reaction steps involved in the oxidation of the main thiophene-OH adduct by O_2 satisfy Hammond's principle: the transition state involved in the formation of the R1-5OO-*syn* radical is structurally closer to the product than the transition state involved in the formation of the R1-3OO-*syn* radical.

The calculated energy profiles have been supplemented with calculations of kinetic rate constants and branching ratios under atmospheric pressure and in the fall-off regime, down to pressure of 10^{-10} bar, using conventional TST and RRKM theories. Comparison with the results of calculations employing variational transition state theory (VTST) as benchmark kinetic model indicates that TST and RRKM theories result in overestimation of the obtained kinetic rate constants by, at most, one order of magnitude. The supplied data indicate that, under a kinetic control of the reaction, the most abundant product resulting from the oxidation of the $[C_4H_4S\text{-}OH]^{\bullet}$ adduct by O_2 is also the R1-5OO-*syn* radical. For the *anti* modes as well, O_2 addition at the C_5 position is also both thermodynamically and kinetically favored over addition at the C_3 position. At last, the computed branching ratios indicate that the regioselectivity of the reaction decreases with increasing temperatures and decreasing pressures.

Acknowledgements

A. Shiroudi acknowledges a PhD fellowship from the "Bijzonder Onderzoeksfonds" (BOF) of Hasselt University. All calculations presented in this work have been performed at the Flemish Supercomputer Center (Vlaams Supercomputer Centrum). This cluster has been financed by budgets obtained from the Katholieke Universiteit Leuven, as well as from individual contributions by users, and funding obtained from the Hercules foundation and the Flemish government.

Supplementary material

Supplementary data (Tables S1−S3) associated with this article can be found, in the online version. Table S1: Effective rate constants (in cm^3 $molecule^{-1}$ s^{-1}) for the reported reaction channels obtained by means of RRKM theory at different pressures and temperatures, according to the computed UM06-2*x*/aug-cc-pVTZ energy profiles (*x*=1,3 and *y*=2,4); Table S2: Kinetic rate constants (in s^{-1}), effective rate constants, and branching ratios for all reaction steps involved in the reported chemical pathways at ambient temperature and different pressures using the RRKM theory, according to the computed UM06-2*x*/aug-cc-pVTZ energy profiles (*z*=1−4); Table S3: Dependence upon the pressure and temperature of the regioselectivities [RSI=*R*(**3**)−*R*(**1**)/*R*(**1**)+*R*(**3**)] and [RSI= *R*(**4**)−*R*(**2**)/*R*(**2**)+*R*(**4**)] of O_2 addition in *syn* and *anti* modes onto the thiophene−OH adduct $[C_4H_4S\text{-}OH]^{\bullet}$, according to the RRKM estimates of effective rate constants [k_{eff}(**1**), k_{eff}(**2**), k_{eff}(**3**), k_{eff}(**4**)].

References

[1] W. Brack, A. Schirmer, Environ. Sci. Technol. 37 (2003) 3062.

[2] U. Thuβ, P. Popp, C. Ehrlich, W.-D. Kalkoff, J. High. Res. Chromatogr. 23 (2000) 457.

[3] N.E. Moustafa, J.T. Andersson, Fuel. Process. Technol. 92 (2011) 547.

[4] J.T. Andersson, Int. J. Environ. Anal. Chem. 48 (1992) 1.

[5] G. Mouvier, P. Carlier, Physico-Chemical Behavior of Atmospheric Pollutants, 3rd European Symposium, Varese, Italy, 10−12 April, 1984.

[6] R. Atkinson, R.A. Perry, J.N. Pitts Jr., J. Chem. Phys. 66 (1979) 1578.

[7] R. Atkinson, R.A. Perry, J.N. Pitts Jr., Chem. Phys. Lett. 54 (1978) 14.

[8] M.J. Kurylo, Chem. Phys. Lett. 58 (1978) 233.

[9] R.A. Cox, D. Sheppard, Nature 284 (1980) 330.

[10] P.H. Wine, N.M. Kreutter, C.A. Gump, A.R. Ravishankara, J. Phys. Chem. 85 (1981) 2660.

[11] J.H. Lee, I.N. Tang, J. Chem. Phys. 78 (1983) 6646.

[12] H. MacLeod, G. Poulet, G. Le Bras, J. Chim. Phys. 80 (1983) 287.

[13] R. Atkinson, J.N. Pitts Jr., S.M. Aschmann, J. Phys. Chem. 88 (1984) 1584.

[14] B.J. Finlayson-Pitts, J.N. Pitts Jr., Adv. Environ. Sci. Technol. 7 (1977) 75.

[15] D.G. Hendry, R.A. Kenley, Atmospheric Reaction Products of Organic Compounds, EPA-560/12-79-001, June, 1979.

[16] J.T. Herron, R.E. Huie, J.A. Hodgeson, Chemical Kinetic Data Needs for Modeling the Lower Troposphere, NBS Spec, Publ. 557, Washington, August, 1979.

[17] N.J. Bunce, L. Liu, J. Zhu, D.A. Lane, Environ. Sci. Technol. 31 (1997) 2252.

[18] R. Atkinson, J. Arey, Environ. Health Perspect. 102 (1994) 117.

[19] H. MacLeod, J.L. Jourdain, G. Poulet, G. Le Bars, Atmos. Environ. 18 (1984) 2621.

[20] X. Qu, Q. Zhang, W. Wang, Chem. Phys. Lett. 429 (2006) 77.

[21] J.E. Sickles, W.C. Eaton, L.A. Ripperton, R.S. Wright, Literature Survey of Emissions Associated with Emerging Energy Technologies, EPA report 600/7-77-104, 1977.

[22] D. Lucas, N.J. Brown, Combust. Flame. 49 (1983) 283.

[23] R. Atkinson, J. Phys. Chem. Ref. Data, Monograph 1 (1989) 1.

[24] R. Atkinson, E.C. Tuazon, J. Arey, Int. J. Chem. Kinet. 22 (1990) 1071.

[25] R. Atkinson, J. Phys. Chem. Ref. Data, Monograph 20 (1991) 459.

[26] R. Atkinson, E.C. Tuazon, I. Bridier, J. Arey, Int. J. Chem. Kinet. 26 (1994) 605.

[27] J. Sasaki, S.M. Aschmann, E.S.C. Kwok, R. Atkinson, J. Arey, Environ. Sci. Technol. 31 (1997) 3173.

[28] K. Lorenz, R. Zellner, Ber. Bunsen-Ges. Phys. Chem. 87 (1983) 629.

[29] R. Atkinson, J. Arey, Polycyclic Aromat. Compd. 27 (2007) 15.

[30] R. Atkinson, J. Arey, Chem. Rev. 103 (2003) 4605.

[31] C. Bloss, V. Wagner, M.E. Jenkin, R. Volkamer, W.J. Bloss, J.D. Lee, D.E. Heard, K. Wirtz, M. Martin-Reviejo, G. Rea, J.C. Wenger, M.J. Pilling, Atmos. Chem. Phys. 5 (2005) 641.

[32] R. Koch, R. Knispel, M. Elend, M. Siese, C. Zetzsch, Atmos. Chem. Phys. 7 (2007) 2057.

[33] A. Shiroudi, M.S. Deleuze, J. Mol. Model. 21 (2015) 301.

[34] B. Bohn, C. Zetzsch, Phys. Chem. Chem. Phys. 1 (1999) 5097.

[35] D. Johnson, S. Raoult, M.T. Rayez, J.C. Rayez, R. Lesclaux, Phys. Chem. Chem. Phys. 4 (2002) 4678.

[36] S.Y. Grebenkin, L.N. Krasnoperov, J. Phys. Chem. A 108 (2004) 1953.

[37] S. Raoult, M.T. Rayez, J.C. Rayez, R. Lesclaux, Phys. Chem. Chem. Phys. 6 (2004) 2245.

[38] A. Shiroudi, M.S. Deleuze, S. Canneaux, Phys. Chem. Chem. Phys. 17 (2015) 13719.

[39] B. Bohn, J. Phys. Chem. A 105 (2001) 6092.

[40] H. Eyring, J. Chem. Phys. 3 (1935) 107.

[41] H.S. Johnston, Gas Phase Reaction Rate Theory, Roland Press Co., New York, 1966.

[42] K.J. Laidler, Theories of Chemical Reaction Rates, McGraw-Hill, New York, 1969.

[43] R.E. Weston, H.A. Schwartz, Chemical Kinetics, Prentice-Hall, New York, 1972.

[44] D. Rapp, Statistical Mechanics, Holt, Rinehart, and Winston, New York, 1972.

[45] E.E. Nikitin, Theory of Elementary Atomic and Molecular Processes in Gases, Clarendon Press, Oxford, 1974.

[46] I.W.M. Smith, Kinetics and Dynamics of Elementary Gas Reactions, Butterworths, London, 1980.

[47] J.I. Steinfeld, J.S. Francisco, W.L. Hase, Chemical Kinetics and Dynamics, Prentice-Hall, Englewood Cliffs, NJ, 1989.

[48] G. Lendvay, J. Phys. Chem. 93 (1989) 4422.

[49] A.E. Reed, L.A. Curtiss, F. Weinhold, Chem. Rev. 88 (1988) 899.

[50] V. Lopez, J. Quijano, S. Luna, P. Ruiz, D. Rios, W. Parra, E. Zapata, J. Gaviria, R. Notario, Struct. Chem. 24 (2013) 1811.

[51] J.D. Chai, M. Head-Gordon, Phys. Chem. Chem. Phys. 10 (2008) 6615.

[52] Y. Zhao, D.G. Truhlar, Acc. Chem. Res. 41 (2008) 157.

[53] Y. Zhao, D.G. Truhlar, Theor. Chem. Acc. 120 (2008) 215.

[54] T.H. Dunning, J. Chem. Phys. 90 (1989) 1007.

[55] A.E. Reed, R.B. Weinstock, J. Chem. Phys. 83 (1985) 735.

[56] J.K. Badenhoop, F. Weinhold, Int. J. Quantum. Chem. 72 (1999) 269.

[57] M.J. Frisch, G.W. Trucks, H.B. Schlegel, G.E. Scuseria, M.A. Robb, J.R. Cheeseman, J.A. Montgomery, Jr., T. Vreven, K.N. Kudin, J.C. Burant, J.M. Millam, S.S. Iyengar, J. Tomasi, V. Barone, B. Mennucci, M. Cossi, G. Scalmani, N. Rega, G.A. Petersson, H. Nakatsuji, M. Hada, M. Ehara, K. Toyota, R. Fukuda, J. Hasegawa, M. Ishida, T. Nakajima, Y. Honda, O. Kitao, H, Nakai, M. Klene, X. Li, J.E. Knox, H.P. Hratchian, J.B. Cross, C. Adamo, J. Jaramillo, R. Gomperts, R.E. Stratmann, O. Yazyev, A.J. Austin, R. Cammi, C. Pomelli, J.W. Ochterski, P.Y. Ayala, K. Morokuma, G.A. Voth, P. Salvador, J.J. Dannenberg, V.G. Zakrzewski, S. Dapprich, A.D. Daniels, M.C. Strain, O. Farkas, D.K. Malick, A.D. Rabuck, K. Raghavachari, J.B. Foresman, J.V. Ortiz, Q. Cui, A.G.

Baboul, S. Clifford, J. Cioslowski, B.B. Stefanov, G. Liu, A. Liashenko, P. Piskorz, I. Komaromi, R.L. Martin, D.J. Fox, T. Keith, M.A. Al-Laham, C.Y. Peng, A. Nanayakkara, M. Challacombe, P.M.W. Gill, B. Johnson, W. Chen, M.W. Wong, C. Gonzalez, J.A. Pople, Gaussian 09 Inc, Wallingford, CT, USA, Gaussian Inc, Wallingford, CT, 2009.

[58] I.I.R. Dennington, T. Keith, J. Millam, K. Eppinnett, W.L. Hovell, R. Gilliland, GaussView, Version 3.09; Semichem, Inc., Shawnee Mission, KS, 2003.

[59] C. Gonzalez, H.B. Schlegel, J. Chem. Phys. 90 (1989) 2154.

[60] J.W. McIver Jr., Acc. Chem. Res. 7 (1974) 72.

[61] F. Fukui, J. Phys. Chem. 74 (1970) 4161.

[62] D.A. McQuarrie, Statistical Mechanics, Harper and Row, New York, 1976.

[63] G.H. Herzberg, Molecular Spectra and Molecular Structure. II Infrared and Raman Spectra of Polyatomic Molecules, Van Nostrand Reinhold, New York, 1945.

[64] D.L. Singleton, R.J. Cvetanovic, J. Am. Chem. Soc. 98 (1976) 6812.

[65] R.G. Mortimer, Physical Chemistry, 3rd ed., Elsevier Academic Press, Burlington, 2008.

[66] R. Chang, Physical Chemistry for the Biosciences, University Science Books, Sausalito, California, 2005.

[67] J.W. Moore, R.G. Pearson, Kinetics and Mechanism-The Study of Homogeneous Chemical Reactions, 3rd ed., Wiley, New York, 1981.

[68] H.H. Carstensen, A.M. Dean, O. Deutschmann, Proc. Combust. Inst. 31 (2007) 149.

[69] E.P. Wigner, Z. Phys. Chem. B 19 (1932) 203.

[70] E. Vanden-Eijnden, F.A. Tal, J. Chem. Phys. 123 (2005) 184103.

[71] B.C. Garret, D.G. Truhlar, R.S. Grev, A.W. Magnuson, J. Phys. Chem. 84 (1980) 1730.

[72] B.C. Garret, D.G. Truhlar, J. Am. Chem. Soc. 101 (1979) 4534.

[73] P.J. Robinson, K.A. Holbrook, Unimolecular Reactions, Wiley, New York, 1972.

[74] E. Eyring, S.H. Lin, S.M. Lin, Basic Chemical Kinetics, Wiley, New York, 1980.

[75] S. Canneaux, F. Bohr, E. Henon, J. Comput. Chem. 35 (2014) 82.

[76] J. Troe, J. Chem. Phys. 66 (1977) 4758.

[77] F. Rosas, R.M. Dominguez, M. Tosta, J.R. Mora, E. Marquez, T. Cordova, G. Chuchani, J. Phys. Org. Chem. 23 (2010) 743.

[78] F.M. Mourits, H.A. Rummens, Can J. Chem. 55 (1977) 3007.

[79] J.P. Pellitero, P. Ungerer, A.D. Mackie, J. Phys. Chem. B 111 (2007) 4460.

[80] J. Horiuti, Bull. Chem. Soc. Jpn. 13 (1938) 210.

[81] J.C. Keck, J. Chem. Phys. 32 (1960) 1035.

[82] J.C. Keck, Adv. Chem. Phys. 13 (1967) 85.

[83] D.G. Truhlar, B.C. Garrett, Annu. Rev. Phys. Chem. 35 (1984) 159.

[84] B.C. Garrett, D.G. Truhlar, J. Phys. Chem. 83 (1979) 1052.

[85] B.C. Garrett, D.G. Truhlar, J. Chem. Phys. 70 (1979) 1593.

[86] D.G. Truhlar, B.C. Garrett, Acc. Chem. Res. 13 (1980) 440.

[87] M.G. Evans, M. Polanyi, Trans. Faraday Soc. 34 (1938) 11.

[88] D.G. Truhlar, A.D. Isaacson, B.C. Garrett, Generalized Transition State Theory, in Theory of Chemical Reaction Dynamics (Ed. M. Baer), CRC Press, Boca Raton, FL, Vol. 4, pp. 65−137, 1985.

[89] T. Baer, W.L. Hase, Unimolecular Reaction Dynamics, Oxford University Press, Oxford, 1996.

[90] B.C. Garrett, D.G. Truhlar, J. Phys. Chem. 83 (1979) 1079.

[91] R.G. Gilbert, S.C. Smith, Theory of Unimolecular and Recombination Reactions, Blackwell Scientific, Oxford, 1990.

[92] S.J. Klippenstein, Y.-C. Yang, V. Ryzhov, R.C. Dunbar, J. Chem. Phys. 104 (1996) 4502.

[93] D.M. Wardlaw, R.A. Marcus, Adv. Chem. Phys. 70 (1988) 231.

[94] W.L. Hase, D.M. Wardlaw, Bimolecular Collisions, in Advances in Gas-Phase Photochemistry and Kinetics (Eds. M.N.R. Ashfold, J.E. Baggott), Royal Society of Chemistry, London, 1989.

[95] S.J. Klippenstein, The Chemical Dynamics and Kinetics of Small Radicals, in Advanced Series in Physical Chemistry (Eds. K. Liu, A.F. Wagner), World Scientific, Singapore, Vol. 1, 1995.

[96] C.A. Taatjes, S.J. Klippenstein, J. Phys. Chem. A 105 (2001) 8567.

[97] A.D. Isaacson, D.G. Truhlar, S.N. Rai, R. Steckler, G.C. Hancock, B.C. Garrett, M.J. Redmon, Comput. Phys. Commun. 1987, 47, 91.

[98] Y.A. Borisov, E.E. Arcia, S.L. Mielke, B.C. Garrett, T.H. Dunning Jr., J. Phys. Chem. A 105 (2001) 7724.

[99] I. García-Cruzl, M. Castro, A. Vivier-Bunge, J. Comput. Chem. 21 (2000) 716.

[100] N. Agmon, R.D. Levine, Chem. Phys. Lett. 52 (1977) 197.

[101] J.E. Carpenter, F. Weinhold, J. Mol. Struct. (THEOCHEM) 169 (1988) 41.
[102] A. Shiroudi, M.S. Deleuze, S. Canneaux, J. Phys. Chem. A 118 (2014) 4593.

Graphical Table of Contents

Reaction mechanisms and kinetics of the O_2 addition pathways upon the main thiophene-OH adduct: A theoretical study

Abolfazl Shiroudi and Michael S. Deleuze

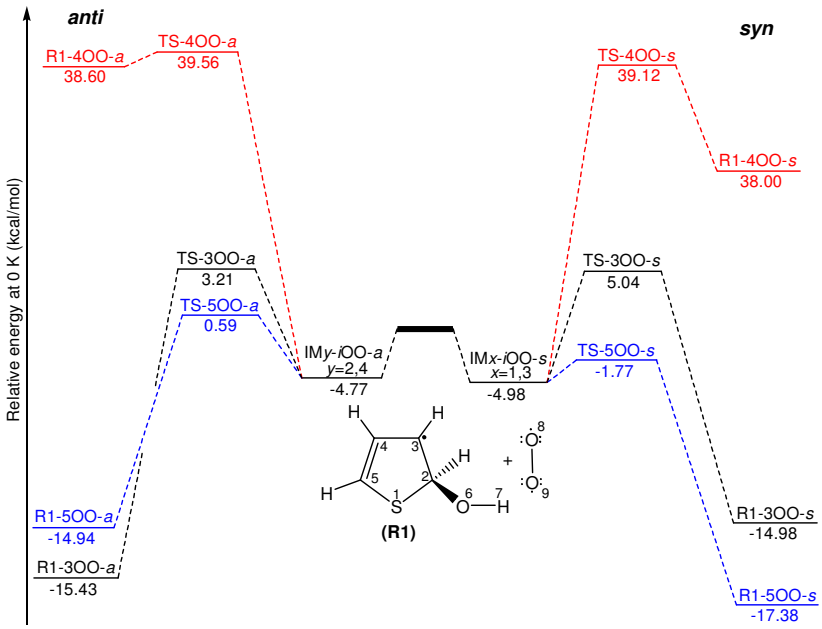

Density functional theory (DFT) methods (ωB97XD and UM06-2x) has been used to study the reaction mechanisms and kinetics of the main (kinetically dominant) thiophene-OH adduct (R1) by triplet molecular oxygen from *syn* and *anti*-directions at C_3, C_4 and C_5-positions. Kinetic parameters under atmospheric pressure and in the fall-off regime have been calculated using transition state theory (TST), variational TST and Rice-Ramsperger-Kassel-Marcus (RRKM) theory. From both thermodynamic and kinetic viewpoints, the most favorable process is O_2 addition at the C_5 position in *syn* mode.